# Spatiotemporal Distribution of β-Amyloid in Alzheimer Disease Is the Result of Heterogeneous Regional Carrying Capacities

Alex Whittington[1], David J. Sharp[1], and Roger N. Gunn[1–3] for the Alzheimer's Disease Neuroimaging Initiative

*[1]Division of Brain Sciences, Imperial College London, Hammersmith Hospital Campus, London, United Kingdom; [2]Imanova Ltd., London, United Kingdom; and [3]Department of Engineering Science, Institute of Biomedical Engineering, University of Oxford, Oxford, United Kingdom*

β-amyloid (Aβ) accumulation in the brain is 1 of 2 pathologic hallmarks of Alzheimer disease (AD), and the spatial distribution of Aβ has been studied extensively ex vivo. **Methods:** We applied mathematical modeling to Aβ in vivo PET imaging data to investigate competing theories of Aβ spread in AD. **Results:** Our results provided evidence that Aβ accumulation starts in all brain regions simultaneously and that its spatiotemporal distribution is due to heterogeneous regional carrying capacities (regional maximum possible concentration of Aβ) for the aggregated protein rather than to longer-term spreading from seed regions. **Conclusion:** The in vivo spatiotemporal distribution of Aβ in AD can be mathematically modeled using a logistic growth model in which the Aβ carrying capacity is heterogeneous across the brain but the exponential growth rate and time of half maximal Aβ concentration are constant.

**Key Words:** image processing; PET/CT; β-amyloid; Alzheimer disease; mathematical modeling; neuroimaging

**J Nucl Med 2018; 59:822–827**
DOI: 10.2967/jnumed.117.194720

The major constituent of neuritic plaques, which appear to play a key role in the pathogenesis of Alzheimer disease (AD) (*1–3*), is β-amyloid (Aβ) (*4,5*). The spatiotemporal distribution of Aβ in AD has been extensively characterized ex vivo through neuropathologic studies using Aβ immunostaining (*6–8*). A consistent spatiotemporal distribution is observed with Aβ, initially restricted to a small number of brain regions before becoming widespread later in the disease (*6,8*). There are competing hypotheses for the biologic mechanism causing the evolution of Aβ pathology. One hypothesis is that Aβ accumulation is determined by properties of the local tissue environment (*9–12*). A second hypothesis is that Aβ originates in a small number of seed regions and, over the duration of the disease, spreads to other brain regions by means such as prion-like self-propagation or transynaptic spread (*7,13–16*).

The in vivo regional Aβ concentration can be measured in humans using PET. Large-cohort cross-sectional studies have been performed (*17,18*), but analysis has focused mainly on classifying the distinct clinical phases of the disease. This approach has provided relatively little information about the way Aβ plaques accumulate over time. Analysis of longitudinal studies has been restricted to either short time windows of no more than 2 years (*19–21*) or the average deposition across the whole cortex (*22*). Thus, despite the large amount of in vivo data collected, the spatiotemporal distribution of Aβ has yet to be fully characterized.

The logistic growth model has been used to model the growth of a wide range of biologic and clinical phenomena, such as the postglacial expansion of forest trees (*23*), the in vitro pharmacodynamics of bactericidal kinetics (*24*), and, most interestingly, in vitro Aβ fibrillation (*25*). Here, we introduce the logistic growth model to provide a mathematical description of a sigmoidal increase in Aβ concentration over time (Fig. 1),

$$\begin{aligned} \mathrm{SUVr}(t) &= \mathrm{NS} + \mathrm{A\beta}(t) \\ &= \mathrm{NS} + \frac{K}{1 + e^{-r(t-T_{50})}}, \end{aligned} \qquad \text{Eq. 1}$$

where $t$ is the time through the accumulation process (a $t$ of 0 corresponds to a time point at which Aβ levels are minimal), SUVr($t$) is the PET Aβ SUV ratio at time $t$, Aβ($t$) is the concentration of Aβ at time $t$, NS is the tracer nonspecific binding, $r$ is the exponential uninhibited growth rate, $T_{50}$ is the time of half-maximal Aβ concentration, and $K$ is the carrying capacity.

It is possible to test between the two competing hypotheses for Aβ accumulation by considering whether each of the 4 model parameters is constant across different brain regions or whether they are regionally different. A summary of the different logistic growth models is displayed in Figure 2. If $T_{50}$ varies between regions, the model is consistent with longer-term spreading from seed regions because seed regions would have a lower $T_{50}$ than other regions (models shown in gray in Fig. 2). If $T_{50}$ is constant across the brain, the model is consistent with local tissue properties driving the accumulation process (models shown in white in Fig. 2). Application of statistical model selection criteria allows us to test between the competing hypotheses.

We took a novel approach to testing between the competing models of Aβ accumulation: we used the whole-cortex Aβ profile derived from the longitudinal study of Jack et al. (in which the patients did not receive any treatment) (*26*) to transform a large cross-sectional study into a chronological dataset by assigning each subject in the cross-sectional dataset a time through the accumulation process. This dataset enabled full spatiotemporal modeling of the Aβ

Received Apr. 11, 2017; revision accepted Oct. 5, 2017.
For correspondence or reprints contact: Roger N. Gunn, Division of Brain Sciences, Burlington Danes Building, Hammersmith Hospital, Du Cane Rd., London, W12 0NN, U.K.
E-mail: r.gunn@imperial.ac.uk
Published online Nov. 16, 2017.

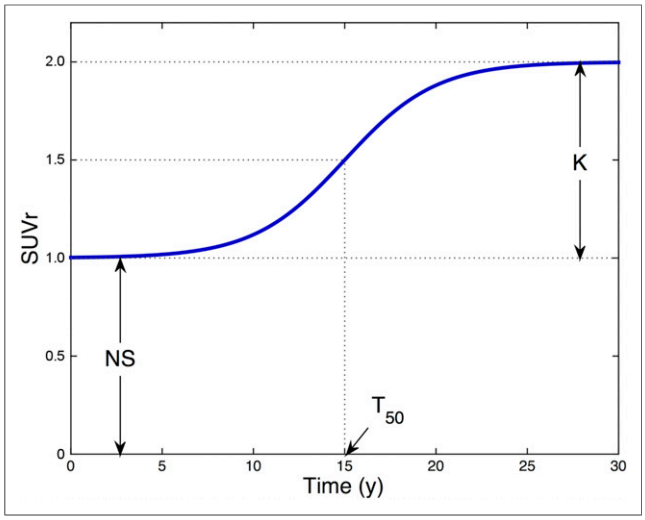


**FIGURE 1.** Logistic growth model describing Aβ PET imaging signal over time as function of PET NS, *K*, $T_{50}$, and *r*.

accumulation process in AD, at a population level. Applying the logistic growth model to in vivo Aβ accumulation in this dataset allowed us to test whether accumulation was best explained by the longer-term spreading of amyloid from seed regions or by heterogeneous regional carrying capacities across brain regions.

## MATERIALS AND METHODS

### Longitudinal Model of Aβ Accumulation

We introduce a logistic growth model to describe the accumulation of Aβ in the human brain. The model assumes that the rate of change of Aβ concentration is proportional to the product of the current concentration of Aβ and a term limiting growth due to the *K* of the local environment. The model is defined by the following differential equation:

$$\frac{d\mathrm{A}\beta(t)}{dt} = r\mathrm{A}\beta(t)\left(1 - \frac{\mathrm{A}\beta(t)}{K}\right). \qquad \text{Eq. 2}$$

Solving the differential equation yields a function for the concentration of Aβ over time:

$$\mathrm{A}\beta(t) = \frac{K}{1 + e^{-r(t-T_{50})}}. \qquad \text{Eq. 3}$$

In vivo PET amyloid tracers are quantified in terms of the SUVr between a target region containing amyloid and a reference region containing only background NS, and therefore:

$$\mathrm{SUVr}(t) = \mathrm{NS} + \mathrm{A}\beta(t). \qquad \text{Eq. 4}$$

Substituting Equation 3 for Aβ(*t*) into equation 4 yields the bottom line of Equation 1, which describes the temporal evolution of the in vivo PET Aβ signal over time (with the 4 parameters NS, *r*, $T_{50}$, and *K*).

### Imaging Data

A chronological Aβ dataset for the AD disease pathway at the population level was generated by transforming a large cross-sectional Aβ dataset using a population time course for the mean cortical SUVr obtained in a smaller longitudinal study.

Cross-sectional $^{18}$F-AV-45 ((*E*)-4-(2-(6-(2-(2-(2-$^{18}$F-fluoroethoxy)ethoxy)ethoxy)pyridin-3-yl)vinyl)-*N*-methyl benzeneamine) human Aβ PET imaging data and structural MRI data were obtained from the Alzheimer's Disease Neuroimaging Initiative (ADNI) database (*27*) for 779 subjects. The ADNI was launched in 2003 as a public–private partnership, led by Principal Investigator Michael W. Weiner. The primary goal of ADNI has been to test whether serial MRI, PET, testing of other biologic markers, and clinical and neuropsychologic assessment can be combined to measure the progression of mild cognitive impairment and early AD. Up-to-date information can be found online at www.adni-info.org.

*$^{18}$F-AV-45 Human Aβ PET Imaging Data.* Each subject underwent a 20-min $^{18}$F-AV-45 PET scan 50 min after injection (370 ± 37 MBq) according to the standardized ADNI protocol (*28*). Three image preprocessing steps were applied to the data before entry into the ADNI imaging database (http://adni.loni.usc.edu/methods/pet-analysis/). Briefly, 4 late-time 5-min frames were coregistered and averaged. The resulting image was converted to a 160 × 160 × 96 voxel static image with voxel dimension of 1.5 × 1.5 × 1.5 mm. Finally, a gaussian filter of 8 mm in full width at half maximum (corresponding to the lowest-resolution scanner used in the study) was applied. These primary data were downloaded from the ADNI database and used in the subsequent analyses.

*T1-Weighted MRI Data.* All subjects underwent T1-weighted 1.5-T structural MRI; the MR images were downloaded from the ADNI imaging database.

### Image Processing

*Registration of Images into Stereotactic Space.* $^{18}$F-AV-45 data were nonlinearly registered into Montreal Neurological Institute 152 (MNI152) space (*29*) using DARTEL (*30*). Initially, the structural MR images were segmented into gray matter and white matter using SPM12 and registered to a group-average template. The group-average template was then registered to MNI152 space. Each subject's $^{18}$F-AV-45 SUVr image was registered to the corresponding MR image using a rigid-body registration. Finally, the individual's DARTEL flow field and template transformation were applied without modulation, resulting in $^{18}$F-AV-45 images in MNI152 space. The normalized maps

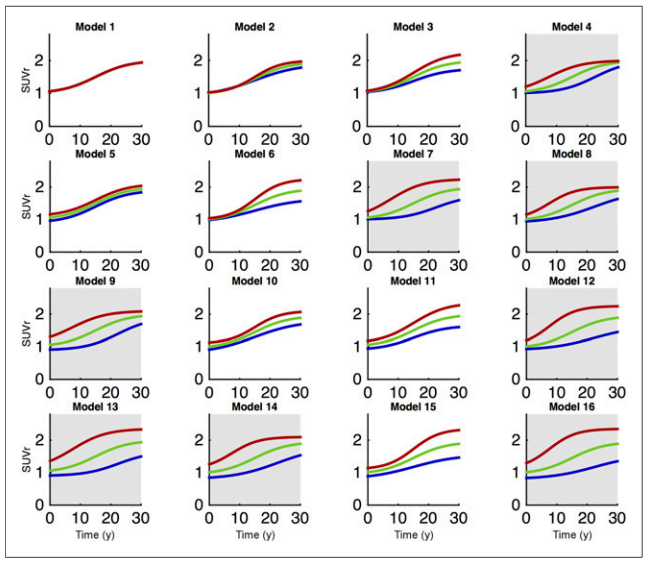


**FIGURE 2.** Sixteen logistic growth models of Aβ accumulation with example curves from 3 distinct brain regions. Models in gray have regionally different $T_{50}$s and are consistent with spreading from seed regions, whereas models in white are consistent with local tissue properties driving Aβ accumulation process.

**TABLE 1**
Subject Characteristics

| Characteristic | Jack et al. (*26*) | ADNI |
|---|---|---|
| Number | 260 | 769 |
| Median age (y) | 79 (range, 70–94) | 73 (range, 55–91) |
| Male patients (*n*) | 162 (62%) | 438 (57%) |
| MCI/AD patients (*n*) | 55 (21%) | 558 (73%) |
| APOE*E4–positive patients (*n*) | 87 (33%) | 342 (44%) |
| Median MMSE score | 28 (range, 23–30) | 28 (range, 19–30) |

MCI = mild cognitive impairment; MMSE = Mini Mental State Examination.

Data from Jack et al. were combined with data from ADNI to create cross-sectional dataset.

were spatially smoothed (gaussian kernel of 8 mm in full width at half maximum). Each registration was visually assessed, with the data of 10 subjects being rejected. Therefore, the final dataset used to construct the chronological data contained 769 subjects.

*Calculation of SUVr Data.* A neuroanatomic atlas (*31*) containing 90 cortical and subcortical regions, and a gray matter probability atlas in MNI152 space, were used to calculate SUVr data. SUVr data were quantified using the gray matter cerebellum as the reference region, which was defined as the intersection between voxels that are in the cerebellum region of interest in the neuroantomic atlas and voxels that have an intensity of over 0.5 in the gray matter probability map. The mean uptake value for the gray matter cerebellum region of interest was obtained, and each image was divided by this mean value to generate an SUVr image for each subject. Finally, the 90 regions of interest were applied to this image to derive regional SUVr data for each subject. Finally, an average cortical SUVr was obtained by calculating the mean SUVr for all 76 cortical regions (weighted by region volume).

### Construction of Population-Level Chronological Aβ Data

Jack et al. (*26*) presented a functional form describing the time course of mean cortical SUVr in AD by integrating rates of change of SUVr in a longitudinal study. Demographics for the study are summarized in Table 1.

*Conversion of Functional Form into $^{18}$F-AV-45 SUVr Units.* The functional form (kindly provided to us by Clifford Jack (*26*)) was derived from longitudinal Aβ imaging data using $^{11}$C-Pittsburgh compound B rather than $^{18}$F-AV-45. Previous work scanning the same subjects with both $^{11}$C-Pittsburgh compound B and $^{18}$F-AV-45 showed that a linear equation can appropriately convert between the different PET tracers (*32–34*): AV-45 SUVr = $a$(Pittsburgh compound B SUVr) + $b$. Therefore, the $^{11}$C-Pittsburgh compound B–derived functional form was transformed into $^{18}$F-AV-45 SUVr units so that the resultant function $\left({}^{\text{Cortex}}_{\text{AV45}}\text{SUV}_\text{r}(t)\right)$ ranged between the mean of the 2.5th and 97.5th cortical $^{18}$F-AV-45 SUVr percentiles for the cross-sectional ADNI dataset ($a$ = 0.72 and $b$ = 0.02). ${}^{\text{Cortex}}_{\text{AV45}}\text{SUV}_\text{r}(t)$ describes the time course of $^{18}$F-AV-45 mean cortical SUVr in AD.

*Timepoint in Chronology of AD.* We used ${}^{\text{Cortex}}_{\text{AV45}}\text{SUV}_\text{r}(t)$ to determine a time in the chronology of AD, $t$, for each of the 769 subjects in the cross-sectional study by calculating their mean cortical SUVr and then finding the value for $t$ from ${}^{\text{Cortex}}_{\text{AV45}}\text{SUV}_\text{r}(t)$ to which that SUVr corresponded in the range 0–30 y. This process generated a chronological dataset at the population level for the spatiotemporal accumulation of Aβ with data at 769 time points over the 30-y disease cascade.

The calculated times were normally distributed, with a mean of 11.8 y and an SD of 5.12 y. It was verified that there was no relationship between the calculated $t$ and SUV in the cerebellum. The test–retest variability of mean cortical $^{18}$F-AV-45 SUVr has been calculated to be less than 3% (*35*). This would translate to a variability of 0.68 y in calculated time through the disease process, for a median SUVr of 1.3.

The coherence of the regional curves in the cross-sectional dataset (Fig. 3) shows not only that there is a stereotypic temporal accumulation at a global level but also that—relative to this stereotypic temporal accumulation—each region has an accumulation curve that is consistent across subjects.

### Regional Analysis of Aβ Accumulation

The logistic growth model of Aβ accumulation (Eq. 1) was then fitted to the chronological data. To determine whether each of the 4 model parameters was constant across the whole brain or varied by region, we investigated 16 different models corresponding to all the permutations of using either global (the parameter is constant across all brain regions) or local (the parameter varies by region) values for each of the 4 model parameters. The full set of models is summarized in Table 2 and contains between 4 and 360 parameters.

Each model was fitted using a nonlinear trust-region reflective algorithm implemented in MATLAB (The MathWorks Inc.) that minimized the residual sum of squared errors subject to an Aβ(0) of less than 0.1 (this constraint did not occur for the optimum model). The Bayesian information criterion (BIC) (*36*) was used to select the most parsimonious model, and the posterior probability that each model was optimum was ascertained from the weights of each model (*37–40*).

### Parametric Image Analysis of Aβ Accumulation

Having identified model 11 (global $r$ and $T_{50}$; local NS and $K$) as optimal on the basis of the regional analysis, we fitted this model at the voxel level to generate parametric images for NS and $K$. Parameter values for $r$ and $T_{50}$ were fixed from the regional analyses, and the

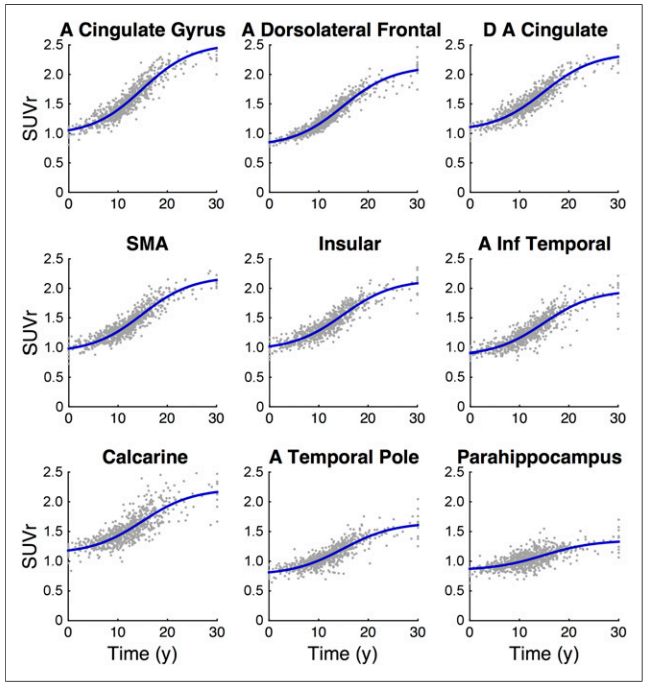


**FIGURE 3.** Model fitting of most parsimonious logistic growth model (model 11) to chronological $^{18}$F-AV-45 Aβ PET data in 9 regions. Model accurately describes data for regions of high (top row), medium (middle row), and low (bottom row) accumulation. A = anterior; D = dorsal; inf = inferior.

**TABLE 2**
Sixteen Parameterizations of Logistic Growth Model of Aβ Accumulation Used to Analyze Chronological $^{18}$F-AV-45 SUVr PET Data at Regional Level

| Model | *K* (SUVr) | *r* ($y^{-1}$) | $T_{50}$ (y) | NS | Parameters | SSQ | $\Delta BIC_i$ |
|---|---|---|---|---|---|---|---|
| 1 | Global | Global | Global | Global | 4 | 3,073.7 | 81,500 |
| 2 | Global | Local | Global | Global | 93 | 2,273.7 | 61,600 |
| 3 | Local | Global | Global | Global | 93 | 1,324.0 | 24,200 |
| 4 | Global | Global | Local | Global | 93 | 1,245.7 | 19,900 |
| 5 | Global | Global | Global | Local | 93 | 1,147.2 | 14,200 |
| 6 | Local | Local | Global | Global | 182 | 1,131.4 | 14,300 |
| 7 | Local | Global | Local | Global | 182 | 1,079.3 | 11,000 |
| 8 | Global | Local | Local | Global | 182 | 1,070.2 | 10,400 |
| 9 | Global | Global | Local | Local | 182 | 1,002.6 | 5,910 |
| 10 | Global | Local | Global | Local | 182 | 977.0 | 4,120 |
| 11 | Local | Global | Global | Local | 182 | 920.6 | 0 |
| 12 | Local | Local | Local | Global | 271 | 1,046.9 | 9,890 |
| 13 | Local | Global | Local | Local | 271 | 918.9 | 865 |
| 14 | Global | Local | Local | Local | 271 | 918.8 | 861 |
| 15 | Local | Local | Global | Local | 271 | 911.0 | 267 |
| 16 | Local | Local | Local | Local | 360 | 908.7 | 1,090 |

SSQ = sum of squared residuals; $\Delta BIC_i$ = difference in BIC between model 11 and all other models.

Ninety cortical and subcortical regions were included, and parameters were either restricted to single value across all regions (global) or fitted individually for each region (local). ΔBIC gives measure of parsimony of each model in relation to smallest BIC value. Model 11 (local *K*, global *r*, global $T_{50}$ and local NS) gives most parsimonious fit to data.

individual voxel time course was fitted using a linearization of the model (supplemental material, available at http://jnm.snmjournals.org).

## RESULTS

### Chronological Aβ Dataset

A chronological Aβ $^{18}$F-AV-45 dataset was created in stereotactic space from 769 subjects who ranged from healthy individuals to AD patients. The chronological data exhibited coherent but different trajectories within individual regions, providing evidence of a stereotypic spatiotemporal distribution at the population level (Fig. 3).

### Model Selection and Implications

Each of the logistic growth models was fitted to the chronological in vivo PET data at a regional level to investigate the spatiotemporal evolution of the Aβ signal in the AD process. The 16 logistic growth models were successfully fitted, and model 11 was identified as the most parsimonious description of the data as determined by the BIC model selection criteria (Table 1). The difference in BIC between model 11 and all the other models was at least 267. Evidence is considered strong when the difference in BIC is greater than 10 (*41*). The posterior probability that model 11 is the best choice was also high ($P > 0.999999$). The model accurately describes the time course of Aβ accumulation in all regions (Supplemental Figs. 1 and 2). A selection of 9 regions with different levels of Aβ accumulation is displayed in Figure 3, demonstrating the ability of the model to accurately describe distinct regional time courses.

Model 11 requires that regional values for *K* and tracer NS vary. In contrast, $T_{50}$ and *r* are constant across brain regions in this model. This suggests that regional variability in Aβ carrying capacities determines the distribution of Aβ concentration, because regions with higher carrying capacities will accumulate more amyloid over time. These results support the hypothesis that Aβ accumulation is limited by properties of the local tissue environment. The observation that the data are best explained by a model with a global $T_{50}$ provides evidence against the spreading hypothesis, as long-term spreading from seed regions would imply a shorter $T_{50}$ for seed regions and therefore require a model (such as model 12) with a local $T_{50}$.

The analysis process was also run on 2 additional sets of regions of interest: a set of 9 regions of interest that are larger and cover the whole brain, and a parcellation that is restricted to cortical regions. Model 11 was the optimum model for both these alternative analyses (Supplemental Tables 2 and 3).

For model 11, the carrying capacity was highest in the anterior cingulate gyrus, precuneus, and frontal operculum cortex (1.55, 1.50, and 1.46 SUVr units, respectively), intermediate in parts of the frontal cortex and insular cortex (1.13 and 1.19), and low in the thalamus and brain stem (0.48 and 0.38). The global $T_{50}$ was 14.9 y, and the global *r* was 0.20 $y^{-1}$.

### Parametric Imaging of *K*

The regional variation normally seen in AD was predicted when model 11 was fitted at the voxel level using the fixed global values of *r* (0.20 $y^{-1}$) and $T_{50}$ (14.9 y) estimated from the regional analysis. Parametric images were generated for *K* and NS (Fig. 4).

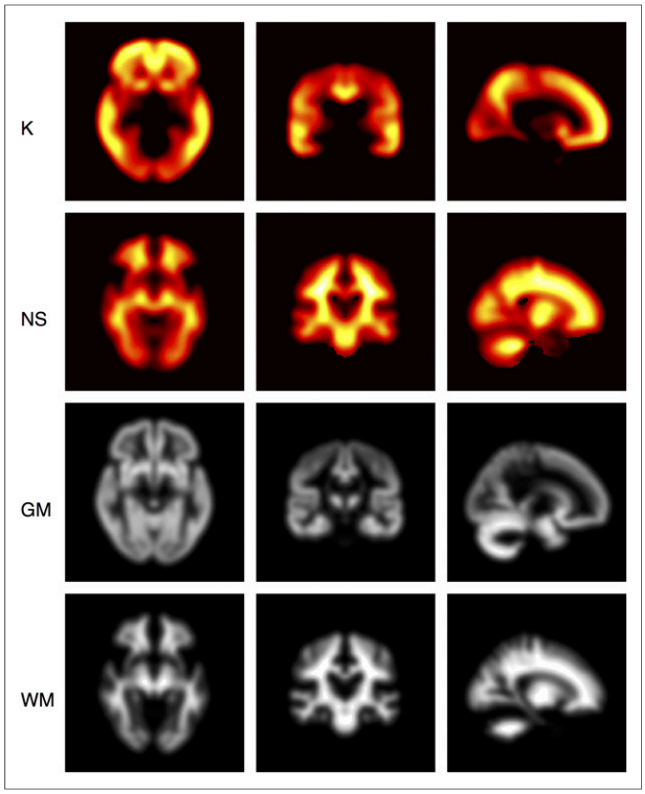


**FIGURE 4.** Parametric images displayed as orthographic projections for *K* and NS obtained from fitting model 11 at voxel level. Gray matter (GM) and white matter (WM) probability maps are displayed for reference. Highest carrying capacities were in frontal lobe, and lowest were in cerebellum, occipital lobe, and brain stem. NS image is consistent with known NS of $^{18}$F-AV-45 to white matter.

## DISCUSSION

Using a logistic growth model, we have mathematically modeled with a high degree of accuracy the spatiotemporal distribution of amyloid in the brain as AD pathology increases. Our results support the hypothesis that regional accumulation of Aβ originates at the same time, and has the same *r,* in all regions. The implication is that the heterogeneous Aβ distribution observed in AD is caused by a property of the local tissue environment rather than by longer-term spreading from seed regions, as the latter would require different values of $r$ or $T_{50}$ (e.g., for long-term spreading, $T_{50}$ would be expected to be earlier in seed regions). If the $T_{50}$ differed in different regions, it would have been impossible to distinguish whether the onset of accumulation occurs at different times in different regions or whether the rate of accumulation differs in different regions. Both mechanisms would require a heterogeneous $T_{50}$ across regions. Because this heterogeneity was not found, one can infer that accumulation begins at the same time and occurs at the same rate in all regions.

Our analysis shows that the spatiotemporal distribution of Aβ at the population level can be accurately modeled using a 4-parameter logistic growth model, where $K$ and NS vary across the brain but $r$ and $T_{50}$ are constant. A model with these characteristics was clearly identified as the most parsimonious model using the BIC model selection criteria. Interestingly, this model has previously been shown to be capable of characterizing the accumulation of Aβ in vitro (*25*).

The current work had some limitations. First, to model the accumulation of Aβ in AD at the population level, we assumed that there is a consistent spatiotemporal distribution for all subjects within the cross-sectional ADNI cohort, which may be an oversimplification. However, the clear coherence of individual trajectories in all brain regions (Supplemental Figs. 1 and 2) and previous postmortem data (*6*) provide confidence that this assumption is reasonable. Second, when creating the cross-sectional dataset, we assumed that all subjects in the longitudinal data and in the cross-sectional study were following the same accumulation trajectory. Table 1 shows demographics for both studies. Both studies have scans from healthy controls, patients with mild cognitive impairment and AD patients, and the subjects are well matched on all characteristics apart from the number of cognitively impaired subjects, which was lower in the longitudinal study. Third, the outcome measure that we have considered (SUVr) does not account for brain atrophy during the 30-y period and the impact that this factor may have on Aβ signal. Studies have shown that the rate of atrophy is greatest in medial temporal regions: 0.6%/y (SD, 0.7) for healthy controls, increasing to 1.5%/y (SD, 0.7) in AD patients (*42*). With these atrophy rates, it is unlikely that atrophy would have a significant impact on the model identification and conclusions presented. Further, it has been shown that atrophy occurs after Aβ accumulates in AD (*43*); therefore, atrophy is not likely to affect our result in this analysis. In the future, it will be important to further investigate the temporal relationship between regional Aβ accumulation and atrophy.

Spatiotemporal modeling of longitudinal data with the logistic growth model introduced here could have much wider utility. The trajectory of Aβ accumulation in dementias and neurodegenerative diseases with different patterns of Aβ needs to be investigated to ascertain whether the temporal process is the same but the topography driven by different regional carrying capacities or whether the accumulation process is actually different.

## CONCLUSION

The in vivo spatiotemporal distribution of Aβ in AD can be mathematically modeled using a logistic growth model in which the Aβ $K$ is heterogeneous across the brain but $r$ and $T_{50}$ are constant. This finding suggests that the heterogeneous Aβ accumulation in AD results from different regional carrying capacities rather than from longer-term spreading from a small number of seed regions.

## DISCLOSURE

Data collection and sharing for this project were funded by the ADNI (National Institutes of Health Grant U01 AG024904) and DOD ADNI (Department of Defense award number W81XWH-12-2-0012). ADNI is funded by the National Institute on Aging and the National Institute of Biomedical Imaging and Bioengineering, as well as through generous contributions from the following: AbbVie, Alzheimer's Association; Alzheimer's Drug Discovery Foundation; Araclon Biotech; BioClinica, Inc.; Biogen; Bristol-Myers Squibb Company; CereSpir, Inc.; Cogstate; Eisai Inc.; Elan Pharmaceuticals, Inc.; Eli Lilly and Company; EuroImmun; F. Hoffmann-La Roche Ltd. and its affiliated company Genentech, Inc.; Fujirebio; GE Healthcare; IXICO Ltd.; Janssen Alzheimer Immunotherapy Research & Development, LLC; Johnson & Johnson Pharmaceutical Research & Development LLC; Lumosity; Lundbeck; Merck & Co., Inc.; Meso Scale Diagnostics, LLC; NeuroRx Research; Neurotrack Technologies; Novartis

Pharmaceuticals Corporation; Pfizer Inc.; Piramal Imaging; Servier; Takeda Pharmaceutical Company; and Transition Therapeutics. The Canadian Institutes of Health Research is providing funds to support ADNI clinical sites in Canada. Private sector contributions are facilitated by the Foundation for the National Institutes of Health (www.fnih.org). The grantee organization is the Northern California Institute for Research and Education. Roger Gunn is a consultant for Abbvie and Cerveau. No other potential conflict of interest relevant to this article was reported.

## ACKNOWLEDGMENTS

Data used in preparation of this article were obtained from the ADNI database (adni.loni.usc.edu). As such, the investigators within the ADNI contributed to the design and implementation of ADNI or provided data but did not participate in analysis or writing of this report. A complete listing of ADNI investigators can be found at https://adni.loni.usc.edu/wp-content/uploads/how_to_apply/ADNI_Acknowledgement_List.pdf. The study was coordinated by the Alzheimer's Therapeutic Research Institute at the University of Southern California. ADNI data are disseminated by the Laboratory for Neuro Imaging at the University of Southern California. We thank Clifford Jack for kindly providing us with the longitudinal mean cortical PET SUVr data; Ilan Rabiner and Paul Matthews for helpful comments on the manuscript; and Yasser Ituria and Alan Evans for interesting discussions on this topic.

## REFERENCES

1. Hardy JA, Higgins GA. Alzheimer's disease: the amyloid cascade hypothesis. *Science.* 1992;256:184–185.
2. Hardy J, Allsop D. Amyloid deposition as the central event in the aetiology of Alzheimer's disease. *Trends Pharmacol Sci.* 1991;12:383–388.
3. Stefani M, Dobson C. Protein aggregation and aggregate toxicity: new insights into protein folding, misfolding diseases and biological evolution. *J Mol Med.* 2003;81:678–699.
4. Glenner GG, Wong CW. Alzheimer's disease: initial report of the purification and characterization of a novel cerebrovascular amyloid protein. *Biochem Biophys Res Commun.* 1984;120:885–890.
5. Wong CW, Quaranta V, Glenner GG. Neuritic plaques and cerebrovascular amyloid in Alzheimer disease are antigenically related. *Proc Natl Acad Sci USA.* 1985;82:8729–8732.
6. Braak H, Braak E. Neuropathological stageing of Alzheimer-related changes. *Acta Neuropathol (Berl).* 1991;82:239–259.
7. Thal DR, Rüb U, Orantes M, Braak H. Phases of Aβ-deposition in the human brain and its relevance for the development of AD. *Neurology.* 2002;58:1791–1800.
8. Arnold SE, Hyman BT, Flory J, Damasio AR, Van Hoesen GW. The topographical and neuroanatomical distribution of neurofibrillary tangles and neuritic plaques in the cerebral cortex of patients with Alzheimer's disease. *Cereb Cortex.* 1991;1:103–116.
9. Buckner RL, Snyder AZ, Shannon BJ, et al. Molecular, structural, and functional characterization of Alzheimer's disease: evidence for a relationship between default activity, amyloid, and memory. *J Neurosci.* 2005;25:7709–7717.
10. Hafkemeijer A, van der Grond J, Rombouts SARB. Imaging the default mode network in aging and dementia. *Biochim Biophys Acta.* 2012;1822:431–441.
11. Braga RM, Sharp DJ, Leeson C, Wise RJS, Leech R. Echoes of the brain within default mode, association, and heteromodal cortices. *J Neurosci.* 2013;33:14031–14039.
12. Buckner RL, Andrews-Hanna JR, Schacter DL. The brain's default network: anatomy, function, and relevance to disease. *Ann N Y Acad Sci.* 2008;1124:1–38.
13. Song HL, Shim S, Kim DH, et al. β-amyloid is transmitted via neuronal connections along axonal membranes. *Ann Neurol.* 2014;75:88–97.
14. Thal DR, Capetillo-Zarate E, Del Tredici K, Braak H. The development of Amyloid beta protein deposits in the aged brain. *Sci Aging Knowledge Environ.* 2006;2006:re1.
15. Nath S, Agholme L, Kurudenkandy FR, Granseth B, Marcusson J, Hallbeck M. Spreading of neurodegenerative pathology via neuron-to-neuron transmission of β-amyloid. *J Neurosci.* 2012;32:8767–8777.
16. Hallbeck M, Nath S, Marcusson J. Neuron-to-neuron transmission of neurodegenerative pathology. *Neuroscientist.* 2013;19:560–566.
17. Rowe CC, Ellis KA, Rimajova M, et al. Amyloid imaging results from the Australian imaging, biomarkers and lifestyle (AIBL) study of aging. *Neurobiol Aging.* 2010;31:1275–1283.
18. Mueller SG, Weiner MW, Thal LJ, et al. Ways toward an early diagnosis in Alzheimer's disease: the Alzheimer's disease neuroimaging initiative (ADNI). *Alzheimers Dement.* 2005;1:55–66.
19. Resnick SM, Sojkova J, Zhou Y, et al. Longitudinal cognitive decline is associated with fibrillar amyloid-beta measured by [$^{11}$C]PiB. *Neurology.* 2010;74:807–815.
20. Landau SM, Fero A, Baker SL, et al. Measurement of longitudinal β-amyloid change with $^{18}$F-florbetapir PET and standardized uptake value ratios. *J Nucl Med.* 2015;56:567–574.
21. Villain N, Chételat G, Grassiot B, et al. Regional dynamics of amyloid-β deposition in healthy elderly, mild cognitive impairment and Alzheimer's disease: a voxelwise PiB-PET longitudinal study. *Brain.* 2012;135:2126–2139.
22. Bateman RJ, Xiong C, Benzinger TL, et al. Clinical and biomarker changes in dominantly inherited Alzheimer's disease. *N Engl J Med.* 2012;367:795–804.
23. Bennett KD. Postglacial population expansion of forest trees in Norfolk, UK. *Nature.* 1983;303:164–167.
24. Yano Y, Oguma T, Nagata H, Sasaki S. Application of logistic growth model to pharmacodynamic analysis of in vitro bactericidal kinetics. *J Pharm Sci.* 1998;87:1177–1183.
25. Lee C-C, Nayak A, Sethuraman A, Belfort G, McRae GJ. A three-stage kinetic model of amyloid fibrillation. *Biophys J.* 2007;92:3448–3458.
26. Jack CRJ, Wiste HJ, Lesnick TG, et al. Brain β-amyloid load approaches a plateau. *Neurology.* 2013;80:890–896.
27. Jagust WJ, Bandy D, Chen K, et al. The Alzheimer's disease neuroimaging initiative positron emission tomography core. *Alzheimers Dement.* 2010;6:221–229.
28. Jagust WJ, Landau SM, Koeppe RA, et al. The Alzheimer's disease neuroimaging initiative 2 PET core: 2015. *Alzheimers Dement.* 2015;11:757–771.
29. Mazziotta J, Toga A, Evans A, et al. A probabilistic atlas and reference system for the human brain: international consortium for brain mapping (ICBM). *Philos Trans R Soc Lond B.* 2001;356:1293–1322.
30. Ashburner J. A fast diffeomorphic image registration algorithm. *Neuroimage.* 2007;38:95–113.
31. Tziortzi AC, Searle GE, Tzimopoulou S, et al. Imaging dopamine receptors in humans with [$^{11}$C]-(+)-PHNO: dissection of D3 signal and anatomy. *Neuroimage.* 2011;54:264–277.
32. Landau SM, Breault C, Joshi AD, et al. Amyloid-β imaging with Pittsburgh compound B and florbetapir: comparing radiotracers and quantification methods. *J Nucl Med.* 2013;54:70–77.
33. Landau SM, Thomas BA, Thurfjell L, et al. Amyloid PET imaging in Alzheimer's disease: a comparison of three radiotracers. *Eur J Nucl Med Mol Imaging.* 2014;41:1398–1407.
34. Wolk DA, Zhang Z, Boudhar S, Clark CM, Pontecorvo MJ, Arnold SE. Amyloid imaging in Alzheimer's disease: comparison of florbetapir and Pittsburgh compound-B positron emission tomography. *J Neurol Neurosurg Psychiatry.* 2012;83:923–926.
35. Joshi AD, Pontecorvo MJ, Clark CM, et al. Performance characteristics of amyloid PET with florbetapir F 18 in patients with Alzheimer's disease and cognitively normal subjects. *J Nucl Med.* 2012;53:378–384.
36. Schwarz G. Estimating the dimension of a model. *Ann Stat.* 1978;6:461–464.
37. Akaike H. A bayesian analysis of the minimum AIC procedure. *Ann Inst Stat Math.* 1978;30:9–14.
38. Akaike H. A bayesian extension of the minimum AIC procedure of autoregressive model fitting. *Biometrika.* 1979;66:237–242.
39. Bozdogan H. Model selection and Akaike's information criterion (AIC): the general theory and its analytical extensions. *Psychometrika.* 1987;52:345–370.
40. Burnham KP, Anderson DR. Multimodel inference: understanding AIC and BIC in model selection. *Sociol Methods Res.* 2004;33:261–304.
41. Kass RE, Raftery AE. Bayes factors. *J Am Stat Assoc.* 1995;90:773–795.
42. Sluimer JD, Flier WM, Karas GB, et al. Accelerating regional atrophy rates in the progression from normal aging to Alzheimer's disease. *Eur Radiol.* 2009;19:2826–2833.
43. Jack CR Jr, Knopman DS, Jagust WJ, et al. Tracking pathophysiological processes in Alzheimer's disease: an updated hypothetical model of dynamic biomarkers. *Lancet Neurol.* 2013;12:207–216.